Reactor field reconstruction from sparse and movable sensors using Voronoi tessellation-assisted convolutional neural networks

He-Lin Gong[1] · Han Li[1] · Dunhui Xiao[2] · Sibo Cheng[3]

Abstract

The aging of operational reactors leads to increased mechanical vibrations in the reactor interior. The vibration of the in-core sensors near their nominal locations is a new problem for neutronic field reconstruction. Current field-reconstruction methods fail to handle spatially moving sensors. In this study, we propose a Voronoi tessellation technique in combination with convolutional neural networks to handle this challenge. Observations from movable in-core sensors were projected onto the same global field structure using Voronoi tessellation, holding the magnitude and location information of the sensors. General convolutional neural networks were used to learn maps from observations to the global field. The proposed method reconstructed multi-physics fields (including fast flux, thermal flux, and power rate) using observations from a single field (such as thermal flux). Numerical tests based on the IAEA benchmark demonstrated the potential of the proposed method in practical engineering applications, particularly within an amplitude of 5 cm around the nominal locations, which led to average relative errors below 5% and 10% in the L_2 and L_∞ norms, respectively.

Keywords Voronoi tessellation · Field reconstruction · Nuclear reactors · Reactor physics · On-line monitoring

1 Introduction

Since its advent in the 1950 s, nuclear energy has been crucial for meeting the world's energy needs and is an important component of clean energy. Nuclear energy is primarily generated through nuclear reactors, which are generally designed to operate for 30–40 years and can last even longer with license renewals. Data from the Power Reactor Information System indicates that among the total of 437 reactors, 289 reactors have been in operation for more than 30 years [1]. Thus, more than 60% of the current nuclear reactors face aging issues, which implies an increase in operational problems or anomalies in reactors. The aging of operational reactors also leads to increased mechanical vibrations of reactor internals, such as core barrels, control rods, in-core instruments, and fuel assemblies, or other vibrations such as flow blockage and coolant inlet perturbations [2–6].

Various reactor core monitoring techniques aim to address these challenges, and they are primarily based on observations of the neutron flux acquired by in-core and ex-core instrumentation combined with numerical simulations. These techniques and systems include CORTEX [7], BEACON [8], and RAINBOW [9]. A detailed overview of reactor core monitoring techniques is available in [10]. Field reconstruction combines observed data in the core and simulation data [11, 12] and aims to determine the neutronic field in the core. Subsequently, safety-related parameters are calculated, such as enthalpy rise hot channel factor, peak heat flux hot channel factor, linear power density of fuel rods, and deviation from nucleate boiling ratio.

✉ Sibo Cheng
  sibo.cheng@imperial.ac.uk

1 Paris Elite Institute of Technology, Shanghai Jiao Tong University, Shanghai 200240, China

2 School of Mathematical Sciences, Tongji University, Shanghai 200092, China

3 Department of Computing, Data Science Institute, Imperial College London, London SW7 2AZ, UK

Data assimilation is a key algorithm for field reconstruction, which originated from earth sciences, including meteorology and oceanography [13]. The data assimilation framework allows the combination of observations and models in an optimal and consistent manner, including information about their uncertainties [14–16]. It has been applied in several studies in nuclear engineering [9, 17–21] for field reconstruction in a unified formalism. Data assimilation with a reduced basis is another framework, which has been extensively researched in recent years [22–32]. In summary, studies on data assimilation have aimed to improve the accuracy, efficiency, and robustness of physical field reconstructions. Further details are available in Ref. [33].

However, as the location of the sensors affects the accuracy and robustness of the reconstructed field, optimization of sensor placement is an important aspect of the study. In [22], the authors proposed a generalized empirical interpolation method (GEIM) [34] to select quasi-optimal sensor locations in the framework of data assimilation and reduced basis, which was validated on three types of operational reactors at Électricité de France (EDF). In [35], simulated annealing was applied to optimize the placement of fixed in-core detectors using variance-based and information entropy-based methods to define the objective function. Recently, clustering methods, such as the K-means algorithm, have been used to optimize in-core detector locations for flux mapping in Advanced Heavy Water Reactor [36, 37]. In a recent study for building nuclear digital twins based on the Transient Reactor Test facility at the Idaho National Laboratory, a greedy algorithm was used to optimize sensor locations on a grid, adhering to user-defined constraints [38]. All these methods attempted to optimize the placement of the in-core detectors in a heuristic manner and were limited to a fixed sensor arrangement similar to that used during the training process. However, research on algorithms for handling detector vibrations is scanty.

The vibration of the in-core sensors near their nominal locations is a new problem that may arise from the aging of operational reactors. A typical limitation is attributed to the inability of all the aforementioned methods to handle spatially moving sensors. Recently, the work of [39] facilitated the practical use of neural networks for global field estimation, considering that sensors could move and become online or offline over time. The Voronoi tessellation [40] was used to obtain a structured-grid representation from sensor locations; subsequently, convolutional neural networks (CNNs) were used to build a map from movable sensors to the physical field. Inspired by this work, we adapted the framework to perform field reconstruction in nuclear reactors, such that the vibration of sensors was considered during the reconstruction of neutronic fields.

The remainder of this paper is organized as follows. In Sect. 2, we provide a detailed description of the methodology

for field reconstruction with movable sensors by using Voronoi tessellation along with convolutional neural networks (V-CNN). In Sect. 3, we present the physical model and the detailed process for neutronic field reconstructing. Section 4 illustrates the numerical results, in which various error metrics have been presented to evaluate the performance of the method. Finally, we provide a brief conclusion and discuss future work in Sect. 5.

2 Methodology for field reconstruction with movable sensors

We aim to reconstruct a two-dimensional (2D) neutronic field $\boldsymbol{\phi} \in \mathbb{R}^{n_x \times n_y}$ in the reactor core domain $\Omega \in \mathbb{R}^2$ from sparse and limited in-core sensor observations $\boldsymbol{y} \in \mathbb{R}^{n_{obs}}$ at location $\boldsymbol{r}_{y_i}$, $i = 1, ..., n_{obs}$. Here, n_{obs} indicates the number of in-core sensor observations, while n_x and n_y denote the number of grid points in the horizontal (x) and vertical (y) directions in a high-resolution field, respectively. Handling movable sensors at their nominal locations in the field are a challenging task. Field reconstruction should be performed using only a single machine learning model to avoid retraining when the sensors move from their nominal locations. This was achieved through two key processes, as described below:

(i) A partition method using Voronoi tessellation which tolerated the local perturbations of sensor locations;
(ii) A machine learning framework that mapped the observations to the global physical field in the same structure.

We note that, considering that the sensors in the core of a reactor were fixed, such as self-powered neutron detectors (SPND), we only considered cases of sensor vibration near their fixed positions, rather than significant movement in the entire domain over time. The latter corresponds to the cases referred to in [39].

In Fig. 1, we present V-CNNs for neutronic field reconstruction and provide a detailed description of each component in the following sections.

2.1 Voronoi tessellation for spatial domain partitions

For reconstruction using movable sensors, Voronoi tessellation is an essential step that maps the observations to the entire spatial domain. For a given space Ω, which is generally in 2D, a set of points $\{\boldsymbol{r}_i, i = 1, ..., n_{obs}\} \in \Omega$. The tessellation approach optimally partitions the given space Ω into n_{obs} regions $G = \{g_1, g_2, ..., g_{n_{obs}}\}$ using the boundaries
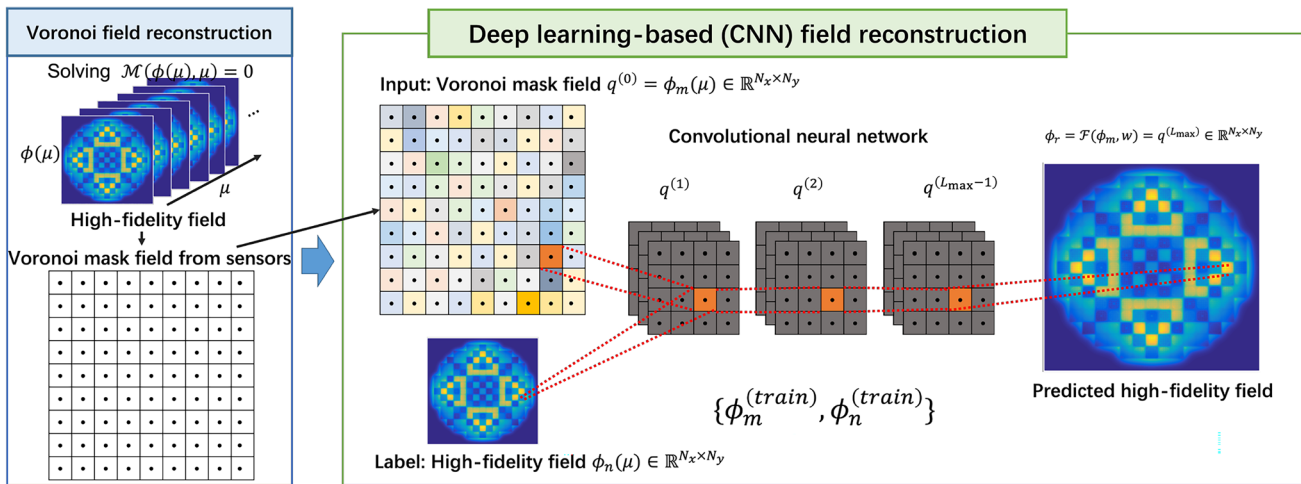
Fig. 1 (Color online) V-CNNs for neutronic field reconstruction from discrete sensor locations in a 2D reactor core. The input Voronoi field is constructed from 81 sensors from each center of fuel assembly. The Voronoi field is then fed into a CNN with the Voronoi mask field ϕ_m, and the output of the CNN is the reconstructed field ϕ_r. In the mask field, a grid with a sensor i (black circle) has a value of $\phi_{m,i}$, which reflects the detected value of the underlying field at site
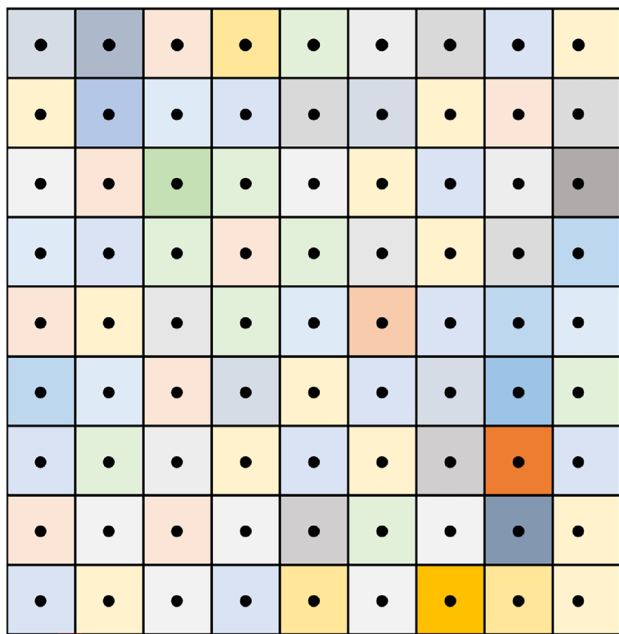

Fig. 2 (Color online) Example of 81 points and the related Voronoi tessellation using Euclidean measure

determined by the measure d among the given points. Using the measure d, Voronoi tessellation can be expressed as

$$g_i = \{r \in \Omega \mid d(r, r_i) < d(r, r_j), j \neq i\}. \tag{1}$$

In this study, the Euclidean measure was used, and the Voronoi boundaries between the points were their bisectors. Figure 2 shows an example of 81 points and the related Voronoi

partitions in the Euclidean measure. The Voronoi tessellation conveniently projects sparse sensor observations to the global physical field. Thus, learning the map from sparse observations to the global field via CNNs is possible. More importantly, this partitioning process can tolerate local perturbations in the sensor locations. For more details on the mathematical theory of the Voronoi tessellation, we refer readers to [40–43].

2.2 Input and output of the machine learning model

To reconstruct the physical field using machine learning, we prepared the input data for the model using the following process:

(i) Determine the sensor locations r_{y_i}, $i = 1, ..., n_{\text{obs}}$ in the reactor core. r_{y_i} may vibrate from its nominal location $r_{y_i}^{\text{nominal}}$. $r_{y_i} = r_{y_i}^{\text{nominal}} + \delta r_{y_i}$, where δr_{y_i} presents the amplitude of the vibration. In the following, for reasons of convenience, we denote δr_{y_i} as δ.

(ii) Calculate the Voronoi tessellation $s_i \in \mathbb{R}^{n_x \times n_y}$ using r_{y_i}, $i = 1, ..., n_{\text{obs}}$. The Voronoi tessellation first partitions the reactor domain Ω into n_{obs} regions $G = \{g_1, ..., g_{n_{\text{obs}}}\}$ with $\Omega = \cup_{i=1}^{n_{\text{obs}}} g_i$, such that each region g_i contains one sensor located at r_{y_i}. s_i is defined as follows:

$$s_i(r) = \begin{cases} 1 & \text{if } r \in g_i \\ 0 & \text{otherwise} \end{cases}. \tag{2}$$

(iii) Prepare the Voronoi mask field $\boldsymbol{\phi}_m \in \mathbb{R}^{n_x \times n_y}$ using Voronoi tessellation $s_i, \; i = 1, ..., n_{\text{obs}}$. The element $\boldsymbol{\phi}_m(\boldsymbol{r})$ satisfies

$$\boldsymbol{\phi}_m(\boldsymbol{r}) = \boldsymbol{y}_{r_i} , \; \text{if } \boldsymbol{r} \in g_i. \tag{3}$$

The Voronoi mask field $\boldsymbol{\phi}_m$ and related target neutronic field $\boldsymbol{\phi}_n$ are provided to a machine learning model $\mathcal{F}_\delta$ such that $\mathcal{F}_\delta : \boldsymbol{\phi}_m \longmapsto \boldsymbol{\phi}_n$, where δ indicates that the model is trained for a given δ. The final output of the model is then denoted by $\boldsymbol{\phi}_r = \mathcal{F}_\delta(\boldsymbol{\phi}_m)$, where the subscript 'r' denotes the reconstructed neutronic field. As the specified input vector contains the observed values and position information of the sensors, the proposed model can handle arbitrary sensor locations and an arbitrary number of sensors.

The perturbations of sensor locations and its impact on the effectiveness of the network were also investigated in this study. The typical amplitude δ of the vibration of sensors in a reactor core is less than 1 cm [6], and we investigated the cases of $\delta = 1$ cm, 3 cm, and 5 cm. The effects of the number and locations of sensors in these scenarios are described in the numerical results section.

To construct the training $\{\phi_m^{(\text{train})}, \phi_n^{(\text{train})}\}$ and test $\{\phi_m^{(\text{test})}, \phi_n^{(\text{test})}\}$ sets for the learning process, a physical model of the underlying problem

$$\mathcal{M}(\phi(\mu), \mu) = 0, \tag{4}$$

was solved numerically. Here, $\mu \in \mathcal{D} \subset \mathbb{R}^p$ denotes the p-dimensional parameter of the model, while $\mathcal{D}$ denotes the feasible parameter domain. The training and test sets were accumulated by solving Eq. (4) over a discrete set $\mathcal{D}^{(\text{discrete})}$ which is representative of $\mathcal{D}$.

2.3 Learning the map using convolutional neural networks

After preparing the input data for the model, a CNN model can be used to learn the map from observations to the field, in the same manner as handling images [44–46]. In this study, the channel of the CNN was set to one, and for each layer, the extraction of t key features of the input data through filtering operations was expressed as

$$q_{ijm}^{(l)} = \sigma \left(\sum_{p=0}^{H-1} \sum_{c=0}^{H-1} q_{i+p-C,j+c-C,m}^{(l-1)} h_{pcm} + b_m \right). \tag{5}$$

Here, $C = \text{floor}(H/2)$, $q^{(l-1)}$ and $q^{(l)}$ are the input and output data at layer l, respectively; h_{pcm} represents a filter of size $H \times H$ and b_m is the bias. $l_{\max}$, H, and m denote the number of layers, filter size, and number of filters, respectively. The output of each filter operation is fed to the activation function $\sigma(\cdot)$ as the output of the neurons. In this study, we selected a rectified linear unit (ReLU) $\sigma(z) = \max(0, z)$ as the

activation function [47]. We used the ADAM optimizer with an early stopping criterion for training and threefold cross-validation [48–50]. Furthermore, the L_2 norm was used to measure the errors in the learning process. The detailed parameters of the CNN used in this study are summarized in Table 1.

The Voronoi mask field $\boldsymbol{\phi}_m \in \mathbb{R}^{n_x \times n_y}$ was used to model $\mathcal{F}$; that is, $q^{(0)} = \boldsymbol{\phi}_m$, and the output of the model was a high-resolution neutronic field $q^{(l_{\max})}$. The learning process is formulated as follows.

$$w = \arg \min_{w} \|q - \mathcal{F}(\boldsymbol{\phi}_m, w)\|_2, \tag{6}$$

where w denotes the model parameters, specifically the filters of the CNN in this study. After completing the training process, the field was reconstructed by feeding the observations y to the model $\mathcal{F}$, i.e., $\boldsymbol{\phi}(y) = \mathcal{F}(\boldsymbol{\phi}_m(y), w)$.

3 Application to neutronic field reconstructions

3.1 Physical model

In this section, the reconstruction method for nuclear reactor cores is tested. We considered a typical benchmark in nuclear reactor physics, namely the 3D IAEA benchmark problem [51] prepared by the Computational Benchmark Problems Committee of the Mathematics and Computation Division of the American Nuclear Society. This benchmark was selected because it is adapted from realistic reactors, and its geometry and composition are much more complex than those of single-region or two-region problems. After completing this test, the method was directly tested based on real reactor calculations.

To test the algorithm, we used the 2D IAEA case, which represents the midplane $z = 190$ cm of the 3D IAEA benchmark see [51, page 437] for a detailed description. The 2D geometry of the reactor is shown in Fig. 3, where only one-quarter is shown because the rest can be inferred from the symmetry along the x and y axes. This quarter is denoted by Ω and comprises four subregions with different physical properties: the first three subregions form the core domain $\Omega_{1,2,3}$, while the fourth subregion is the reflector domain Ω_4. Certain Newman boundary conditions are satisfied on the x and y axes

Table 1 Parameter settings of the CNN

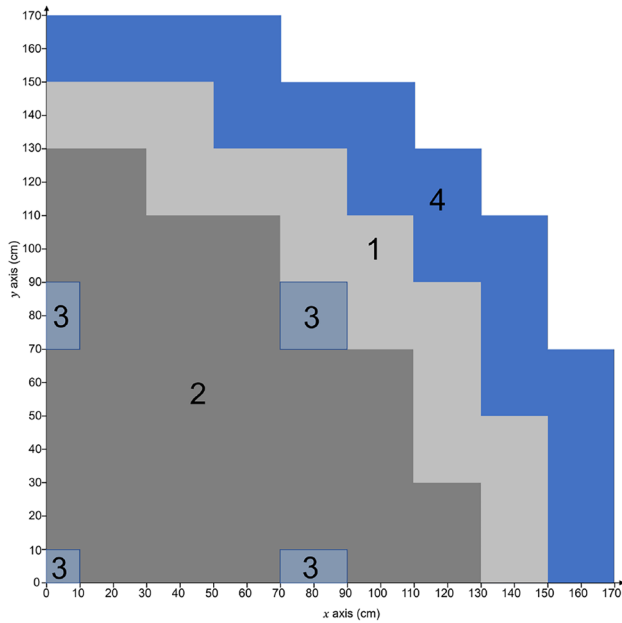| Layers	Hidden	Filter size	Number of filters	Learning rate	Resolution
$l_{\max}$	layers	H	m	of ADAM	$n_x \times n_y$
9	7	8	48	0.0001	171×171

Fig. 3 (Color online) Geometry of the 2D IAEA nuclear core, upper octant: region assignments, lower octant: fuel assembly identification (from [51])

considering symmetry, and the zero-boundary condition is satisfied on the external border, see Fig. 3.

The neutron fields consist of fast and thermal fluxes, that is, $\boldsymbol{\phi} = (\phi_1, \phi_2)$ are modeled using a two-group neutron diffusion equation with suitable boundary conditions. The fluxes are the solutions to the following eigenvalue problem (see [52, 53]): Specifically, the flux ϕ satisfies the following eigenvalue problem: Find $(\lambda, \phi) \in \mathbb{C} \times L^\infty(\Omega) \times L^\infty(\Omega)$, such that

$$\begin{cases} -\nabla(D_1 \nabla \phi_1) + (\Sigma_{a,1} + \Sigma_{1 \to 2} + D_1 B_{z1}^2)\phi_1 = \frac{1}{\lambda}\nu\Sigma_{f,2}\phi_2 \\ -\nabla(D_2 \nabla \phi_2) + (\Sigma_{a,2} + D_2 B_{z2}^2)\phi_2 = \Sigma_{1 \to 2}\phi_1 \end{cases},$$
(7)

with the zero-boundary condition $\phi_i = 0$, $i = 1, 2$ on the external border $\partial\Omega$ and the Newman boundary conditions $\partial(\phi_i)/\partial(\boldsymbol{n}) = 0$, $i = 1, 2$ on axes. The generated nuclear reactor rate $P = \nu\Sigma_{f,1}\phi_1$ reflects the power distribution over the core. The following parameters were used in the above equation:

- D_i: diffusion coefficient of group i with $i \in \{1, 2\}$;
- $\Sigma_{a,i}$: macroscopic absorption cross section of group i;
- $\Sigma_{1 \to 2}$: macroscopic scattering cross section from group 1 to 2;
- $\Sigma_{f,i}$: macroscopic fission cross section of group i;
- ν: average number of neutrons emitted per fission.

The axial buckling $B_{zi}^2 = 0.8 \times 10^{-4}$ for all the regions and energy groups (Table 2). The nominal values of the coefficients in diffusion model (7) are listed in Sect. 3.1.

Under certain mild conditions of the parameters, the maximum eigenvalue λ_{max} is real and strictly positive (see [54, Chapter XXI]). The associated eigenfunction ϕ, which is also real and positive at each point $\mathbf{x} \in \Omega$, and is the flux of interest. In neutronics, the inverse of λ_{max} is conventionally used and is called the multiplication factor

$$k_{eff} := \frac{1}{\lambda_{max}}.$$
(8)

For each parameter setting, k_{eff} is determined by the solution to the eigenvalue problem (7). The maximum eigenvalue λ_{max} is computed using the well-known power method (see [52]). In this study, Freefem++ [55] was used to solve the 2D IAEA benchmark problem. The spatial approximation used $\mathbb{P}_1$ finite elements with a grid size of $h = 1$ cm; thus, the resolution of the field was $n_x \times n_y = 171 \times 171$.

3.2 Field reconstruction

To simulate the variation in the neutronic fields with respect to the parameter variations, we considered the parameters in Sect. 2 as uncertain parameters. Specifically, we assumed the following:

$$\mu = (\mu_1, \mu_2, ..., \mu_n) \in \mathcal{D} = [\mu_{i,nominal} \cdot 0.8, \mu_{i,nominal} \cdot 1.2]^n$$
(9)

where $\mathcal{D}$ is the parameter domain. We randomly generated 10000 samplings of μ in $\mathcal{D}$ and solved Eq. (7) to obtain a collection of 10000 samples of neutronic fields $\mathcal{M} = \{\boldsymbol{\phi}_1(\mu), \boldsymbol{\phi}_2(\mu), \boldsymbol{P}(\mu) \mid \mu \in \mathcal{D}\}$. Among them, 8000, 1000, and 1000 samples were used for training, validation,

Table 2 Parameters of the 2D IAEA benchmark problem

Region	D_1 (cm)	D_2 (cm)	$\Sigma_{1 \to 2}$ (cm^{-1})	$\Sigma_{a,1}$ (cm^{-1})	$\Sigma_{a,2}$ (cm^{-1})	$\nu\Sigma_{f,1}$ (cm^{-1})	$\nu\Sigma_{f,2}$ (cm^{-1})	Material
Ω_1	1.50	0.40	0.02	0.01	0.080	0.00	0.135	Fuel 1
Ω_2	1.50	0.40	0.02	0.01	0.085	0.00	0.135	Fuel 2
Ω_3	1.50	0.40	0.02	0.01	0.130	0.00	0.135	Fuel 2 + Rod
Ω_4	2.00	0.30	0.04	0.00	0.010	0.00	0.000	Reflector

* The axial buckling $B_{zi}^2 = 0.8 \times 10^{-4}$ for all the regions and energy groups

and testing, respectively. We trained three CNN models with the same input data, that is, the thermal flux ϕ_2 which is measurable with in-core detectors, and the output fields, which are the fast flux ϕ_1, thermal flux ϕ_2, and reaction rate P (see Fig. 4 for a schematic).

To synthesize the observations, we assumed that an in-core sensor was located at the center of each assembly to acquire the thermal flux. We further assumed that these sensors could move in a local square with a width δ cm, centered at the center of each assembly. We performed numerical tests for the cases $\delta = 1, 3$, and 5 cm to investigate the effect of different levels of vibration of the sensors. Thus, observations were generated randomly from windows of width δ centered at their nominal locations (see Fig. 5). Then, the model $\mathcal{F}$ was trained based on set $\mathcal{M}$, and schematics of the training process are shown in Figs. 1 and 4.
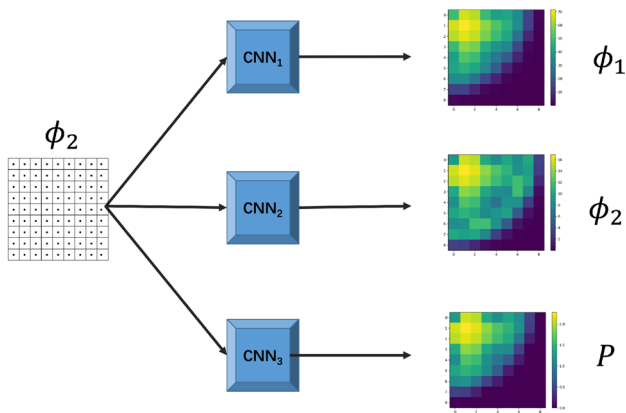

Fig. 4 (Color online) Schematic for the reconstruction of neutronic fields

3.3 Error metrics

Before presenting the numerical results, we define several metrics to evaluate the quality of the field reconstructions. The normalized root-mean-square residual of the difference between the reconstruction ϕ_r and test field ϕ_t is

$$e_2(\phi) := \frac{\|\phi_r - \phi_t\|_2}{\|\phi_t\|_2}. \tag{10}$$

In nuclear engineering, the error in the reconstructed field in L_∞ is another import metric that reflects the worst case scenario for each reconstruction.

$$e_\infty(\phi) := \frac{\|\phi_r - \phi_t\|_{L_\infty}}{\|\phi_t\|_{L_\infty}}. \tag{11}$$

The total average root-mean-square residual and standard deviation over the given test set $\mathcal{M}$ are defined as

$$
\begin{aligned}
E(e_\chi(\phi)) &:= \text{average}_{\phi \in \mathcal{M}}(e_\chi(\phi)) \\
\text{STD}(e_\chi(\phi)) &:= \text{standard deviation}_{\phi \in \mathcal{M}}(e_\chi(\phi)),
\end{aligned} \tag{12}
$$

where χ denotes the L_2 or L_∞ norm.

Furthermore, the average assembly field (fluxes and power rate) and related errors were investigated. The average assembly power is defined as

$$\phi_{\text{ass},k} = \frac{1}{v_k} \int_{v_k} \phi \, dv, \tag{13}$$

where ϕ denotes ϕ_1, ϕ_2 or P, v_k denotes the volume of the k-th subassembly, and k denotes the fuel assemblies, as shown in the lower octant of Fig. 3. The average error $e_2(\phi_{\text{ass}})$, maximum relative error $e_\infty(\phi_{\text{ass}})$, related average $E(e_\chi(\phi_{\text{ass}}))$, and standard deviation $\text{STD}(e_\chi(\phi_{\text{ass}}))$ of the errors over the given test set $\mathcal{M}$ can also be similarly defined.
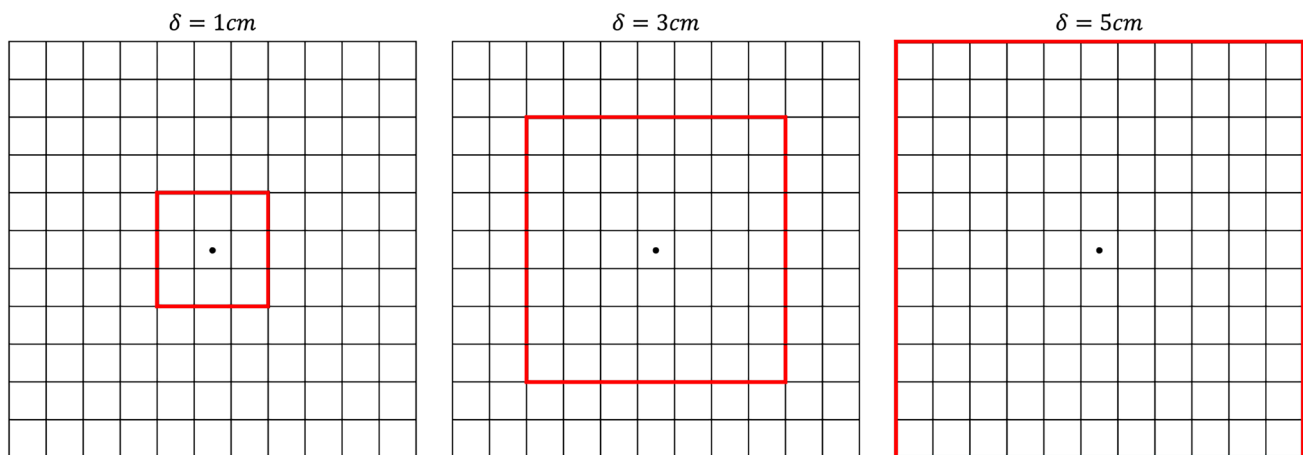

Fig. 5 Different amplitudes of vibrations of a sensor near the nominal location in an assembly

Therefore, we introduce the structural similarity (SSIM) [56] index to measure the field reconstruction. In contrast to the general L_2 error, the SSIM index measures similarity by comparing two images based on luminance, contrast, and structural similarity information.

4 Numerical results

We have described the methodology for field reconstruction with movable sensors using a CNN in Sect. 2 and presented a detailed process for neutronic field reconstruction based on a typical benchmark nuclear engineering domain in Sect. 3. In this section, we describe the numerical performance of the proposed method.

4.1 Performance for the benchmark problem

In Fig. 6, we present the error distributions of the reconstructed fields for different vibration amplitudes, namely $\delta = 1, 3$, and 5 cm, for the 2D IAEA benchmark problem. The reconstruction of ϕ_1 using observations from ϕ_2 performs better than those of ϕ_2 and P. Furthermore, the reconstruction error increases with the amplitude of the vibration, that is, when δ varies from 1 cm to 5 cm. The largest error appears around the interface of the fuel and reflector because of discontinuities in the materials, particularly for the fields of the thermal flux ϕ_2 and the power rate P.

The average assembly values of the reconstructed fluxes and power rate are shown in Fig. 7, and the same conclusions can be drawn. Because of the averaging process, the assembly exhibits considerably smaller relative errors than the pin-wise case.

Three main conclusions can be drawn from analysis of the numerical results.

(i) The proposed V-CNN can reconstruct the multi-field using observations only from thermal flux;
(ii) The reconstruction errors for the assembly are significantly lower than 5%, which is acceptable for engineering applications, i.e., less than 10%, which is an acceptable criterion in reactor physics (more information is available in [57]);
(iii) Even with a movement of amplitude $\delta = 5$ cm for the sensors, the proposed V-CNN reconstructs the field with an error less than 10%.

4.2 Average performance over a test set

To investigate the generalizability of the field reconstruction method, we analyzed the error performance for 1000 test samples. The error metrics were the average relative L_2 error $E(e_2(\phi))$, average relative L_∞ error $E(e_\infty(\phi))$, average relative assembly L_2 error $E(e_2(\phi_{ass}))$, average relative assembly L_∞ error $E(e_\infty(\phi_{ass}))$, average SSIM, $E(SSIM(\phi))$, and the standard deviation of the aforementioned errors.

Table 3 illustrates the numerical results of the errors for the reconstruction of ϕ_1 over the 1000 test samples. All error metrics exhibit good agreement between the reconstructed and original fields. The maximum errors, that is, the L_∞ errors in both the pin-wise and assembly wise cases, are below 2%. The good performance is attributed to the smoothness of the fast flux owing to its relatively longer diffusion length than the thermal flux. Thus, the fast flux is less affected by the heterogeneity of the materials in this benchmark (Fig. 6a for example).

Tables 4 and 5 illustrate the numerical results of the errors for the reconstruction of ϕ_2 and P over the 1000 test samples. The average L_∞ errors in the pin-wise of the thermal flux and power rate were below 10% when the vibration amplitude was less than 3 cm. When the amplitude of the vibration increases, the average L_∞ error exceeds 10%, which unsuitable for practical engineering applications. However, the L_∞ errors are much smaller for the assembly. The worst case occurs for $\delta = 5$ cm when reconstructing ϕ_2, which leads to an error of $E(e_\infty(\phi_{ass})) = 0.0288$ and standard deviation $STD(e_\infty(\phi_{ass})) = 0.0109$. These results further confirm its acceptability for engineering applications. Although the relative L_∞ errors are 10%, most of the points appear around the interface between the fuel and reflector. A relatively large error in this domain is not crucial for safety analysis. Thus, the SSIM indices in all the three tables exceeded 0.99, which further demonstrates the excellent performance for all the field reconstructions.

4.3 Robustness analysis

The robustness of the reconstruction with respect to the number of observations n_{obs} and amount of training data $n_{snapshot}$ was examined. In Fig. 8, we show the dependence of the relative reconstruction errors in L_2 norm and L_∞ norm on $n_{snapshot} = 128, 1280, 4096, 8192, 15743$ and on $n_{obs} = 25, 45, 81$ to recover the thermal flux ϕ_2 over the test set. The number of observations $n_{obs} = 25, 45$, and 81 correspond to sparsities of 0.0855%, 0.154%, and 0.277%, respectively, against the number of grid points in the field. The two figures demonstrate the robustness of the proposed method with respect to the sparsity of the sensors and training data. Few observations and training data lead to low-level reconstruction errors. Furthermore, the addition of training data improves the reconstruction accuracy more significantly than the addition of sensors. This result demonstrates that the proposed field-reconstruction framework is robust against sensor failures and confirms its potential for practical applications.
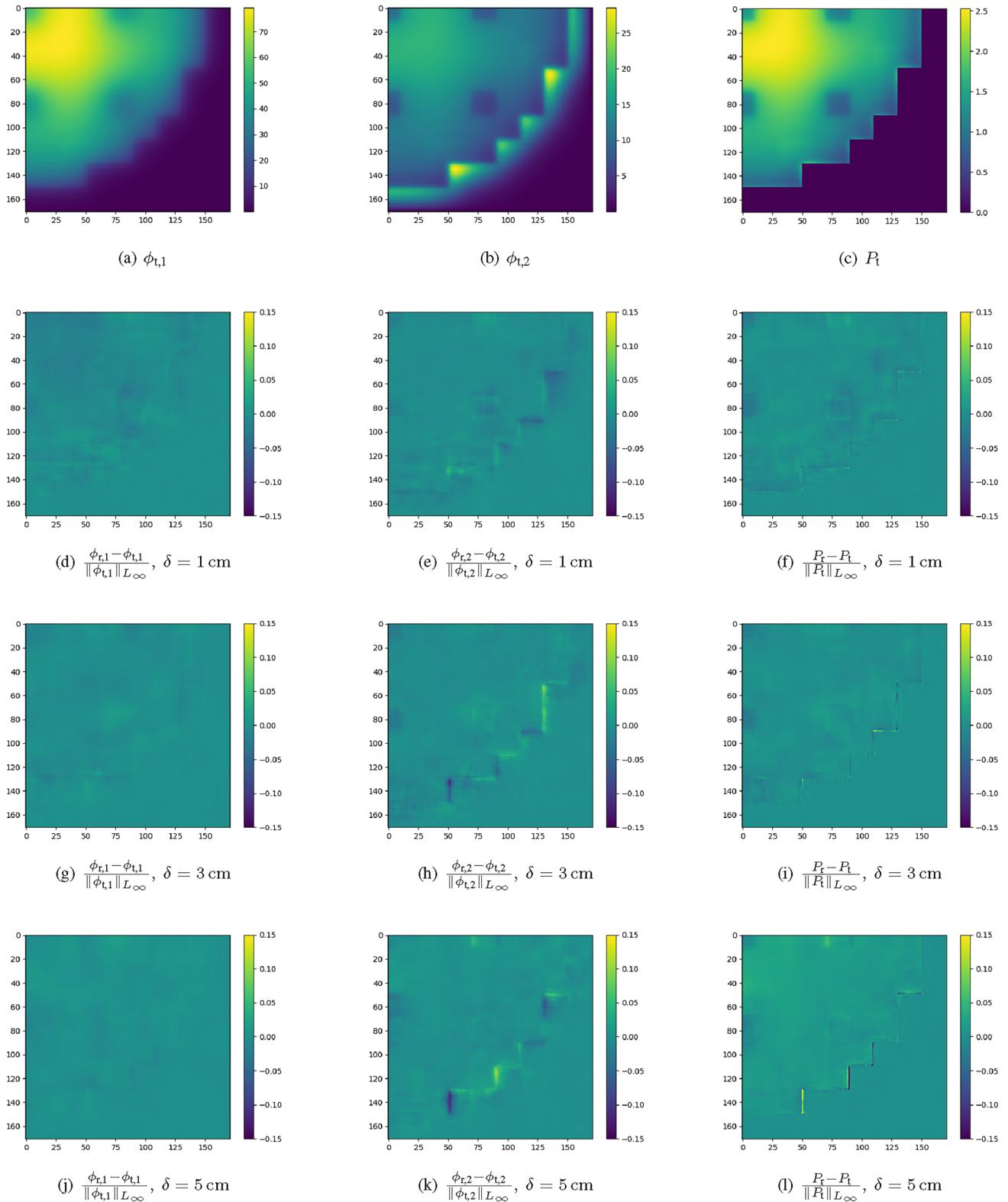
(a) $\phi_{t,1}$

(b) $\phi_{t,2}$

(c) P_t

(d) $\frac{\phi_{r,1}-\phi_{t,1}}{\|\phi_{t,1}\|_{L_\infty}}$, $\delta = 1\,\mathrm{cm}$

(e) $\frac{\phi_{r,2}-\phi_{t,2}}{\|\phi_{t,2}\|_{L_\infty}}$, $\delta = 1\,\mathrm{cm}$

(f) $\frac{P_r-P_t}{\|P_t\|_{L_\infty}}$, $\delta = 1\,\mathrm{cm}$

(g) $\frac{\phi_{r,1}-\phi_{t,1}}{\|\phi_{t,1}\|_{L_\infty}}$, $\delta = 3\,\mathrm{cm}$

(h) $\frac{\phi_{r,2}-\phi_{t,2}}{\|\phi_{t,2}\|_{L_\infty}}$, $\delta = 3\,\mathrm{cm}$

(i) $\frac{P_r-P_t}{\|P_t\|_{L_\infty}}$, $\delta = 3\,\mathrm{cm}$

(j) $\frac{\phi_{r,1}-\phi_{t,1}}{\|\phi_{t,1}\|_{L_\infty}}$, $\delta = 5\,\mathrm{cm}$

(k) $\frac{\phi_{r,2}-\phi_{t,2}}{\|\phi_{t,2}\|_{L_\infty}}$, $\delta = 5\,\mathrm{cm}$

(l) $\frac{P_r-P_t}{\|P_t\|_{L_\infty}}$, $\delta = 5\,\mathrm{cm}$

Fig. 6 (Color online) Reconstructed fields for different vibration amplitudes, $\delta = 1, 3, 5\,\mathrm{cm}$ for the 2D IAEA benchmark problem

(a) $\phi_{\mathrm{ass,t,1}}$

(b) $\phi_{\mathrm{ass,t,2}}$

(c) $P_{\mathrm{ass,t}}$

(d) $\dfrac{\phi_{\mathrm{ass,r,1}}-\phi_{\mathrm{ass,t,1}}}{\|\phi_{\mathrm{ass,t,1}}\|_{L_\infty}},\ \delta = 1\,\mathrm{cm}$

(e) $\dfrac{\phi_{\mathrm{ass,r,2}}-\phi_{\mathrm{ass,t,2}}}{\|\phi_{\mathrm{ass,t,2}}\|_{L_\infty}},\ \delta = 1\,\mathrm{cm}$

(f) $\dfrac{P_{\mathrm{ass,r}}-P_{\mathrm{ass,t}}}{\|P_{\mathrm{ass,t}}\|_{L_\infty}},\ \delta = 1\,\mathrm{cm}$

(g) $\dfrac{\phi_{\mathrm{ass,r,1}}-\phi_{\mathrm{ass,t,1}}}{\|\phi_{\mathrm{ass,t,1}}\|_{L_\infty}},\ \delta = 3\,\mathrm{cm}$

(h) $\dfrac{\phi_{\mathrm{ass,r,2}}-\phi_{\mathrm{ass,t,2}}}{\|\phi_{\mathrm{ass,t,2}}\|_{L_\infty}},\ \delta = 3\,\mathrm{cm}$

(i) $\dfrac{P_{\mathrm{ass,r}}-P_{\mathrm{ass,t}}}{\|P_{\mathrm{ass,t}}\|_{L_\infty}},\ \delta = 3\,\mathrm{cm}$

(j) $\dfrac{\phi_{\mathrm{ass,r,1}}-\phi_{\mathrm{ass,t,1}}}{\|\phi_{\mathrm{ass,t,1}}\|_{L_\infty}},\ \delta = 5\,\mathrm{cm}$

(k) $\dfrac{\phi_{\mathrm{ass,r,2}}-\phi_{\mathrm{ass,t,2}}}{\|\phi_{\mathrm{ass,t,2}}\|_{L_\infty}},\ \delta = 5\,\mathrm{cm}$

(l) $\dfrac{P_{\mathrm{ass,r}}-P_{\mathrm{ass,t}}}{\|P_{\mathrm{ass,t}}\|_{L_\infty}},\ \delta = 5\,\mathrm{cm}$
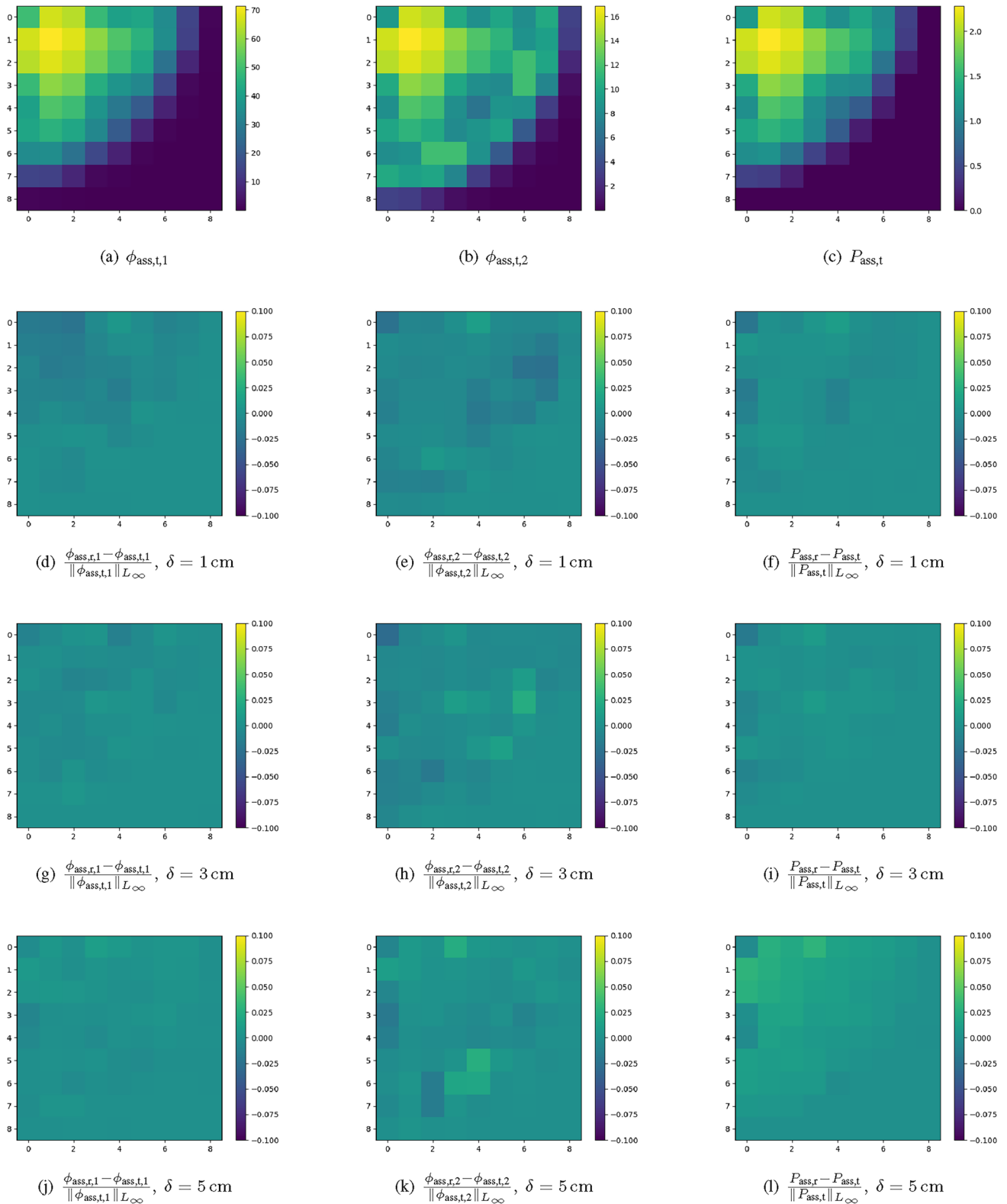
Fig. 7 (Color online) Reconstructed fields in assembly wise for different vibration amplitudes, and $\delta = 1, 3,$ and 5 cm for the 2D IAEA benchmark problem

Table 3 Errors in the different metrics for the reconstruction of ϕ_1 using thermal flux observations from movable sensors

Width	1	3	5
$E(e_2(\phi))$	0.0097	0.0103	0.0119
STD$(e_2(\phi))$	0.0017	0.0020	0.0031
$E(e_\infty(\phi))$	0.0276	0.0293	0.0303
STD$(e_\infty(\phi))$	0.0078	0.0090	0.0091
$E(e_2(\phi_{\mathrm{ass}}))$	0.0084	0.0094	0.0105
STD$(e_2(\phi_{\mathrm{ass}}))$	0.0020	0.0022	0.0032
STD$(e_\infty(\phi_{\mathrm{ass}}))$	0.0155	0.0159	0.0171
$STD(e_\infty(\phi_{\mathrm{ass}}))$	0.0046	0.0054	0.0064
$E(\mathrm{SSIM}(\phi))$	0.9986	0.9982	0.9979
STD$(\mathrm{SSIM}(\phi))$	0.0003	0.0004	0.0004

Table 4 Errors in the different metrics for the reconstruction of ϕ_2 using thermal flux observations from movable sensors

Width	1	3	5
$E(e_2(\phi))$	0.0167	0.0190	0.0213
STD$(e_2(\phi))$	0.0025	0.0032	0.0041
$E(e_\infty(\phi))$	0.0751	0.1001	0.1219
STD$(e_\infty(\phi))$	0.0197	0.0293	0.0391
$E(e_2(\phi_{\mathrm{ass}}))$	0.0120	0.0134	0.0141
STD$(e_2(\phi_{\mathrm{ass}}))$	0.0025	0.0027	0.0028
$E(e_\infty(\phi_{\mathrm{ass}}))$	0.0216	0.0256	0.0288
STD$(e_\infty(\phi_{\mathrm{ass}}))$	0.0085	0.0093	0.0109
$E(\mathrm{SSIM}(\phi))$	0.9969	0.9964	0.9957
STD$(\mathrm{SSIM}(\phi))$	0.0006	0.0008	0.0010

Table 5 Errors in the different metrics for the reconstruction of P using thermal flux observations from movable sensors

Width	1	3	5
$E(e_2(\phi))$	0.0137	0.0164	0.0253
STD$(e_2(\phi))$	0.0031	0.0046	0.0060
$E(e_\infty(\phi))$	0.1429	0.2069	0.2640
STD$(e_\infty(\phi))$	0.0811	0.1079	0.1119
$E(e_2(\phi_{\mathrm{ass}}))$	0.0097	0.0108	0.0192
STD$(e_2(\phi_{\mathrm{ass}}))$	0.0027	0.0037	0.0058
$E(e_\infty(\phi_{\mathrm{ass}}))$	0.0182	0.0191	0.0257
STD$(e_\infty(\phi_{\mathrm{ass}}))$	0.0069	0.0081	0.0082
$E(\mathrm{SSIM}(\phi))$	0.9951	0.9947	0.9920
STD$(\mathrm{SSIM}(\phi))$	0.0012	0.0018	0.0023

To investigate the robustness of the recovery with respect to the observation noise, a noise ϵ_σ that was randomly sampled in the range $(-\sigma, \sigma)$ was added to each clean observation y, thereby generating a noisy observation $y^o = y(1 + \epsilon_\sigma)$ for each sensor. The dependence of the relative reconstruction errors in the L_2 and L_∞ norms of different noise levels, that is, $\sigma = 0.01, 0.02, 0.03, 0.04, 0.05$ for recovering the thermal flux ϕ_2 are shown in Table 6. The test was performed using 81 sensors with a vibration amplitude $\delta = 5$ cm. The errors were first averaged over 100 repeated random observation samplings for each field reconstruction, and then averaged over the test set. On average, the reconstruction error changes significantly for noisy observations. The reconstruction error exhibits a slow linear growth trend with respect to the noise level. Although the L_2 error is below 10%, which is satisfactory for nuclear engineering applications, the L_∞ error remains at approximately 30%, which is unsatisfactory. This provides a direction for further research on reducing the L_∞ error.

5 Conclusion

In this study, a V-CNN was proposed for neutronic field reconstruction to resolve the vibrations of in-core sensors, which may arise from the aging of operational reactors. Observations from movable in-core sensors were projected onto the same global field structure using Voronoi tessellation, holding the magnitude and location information of the sensors. General convolutional neural networks were used to learn maps from observations to the global field. Furthermore, the proposed method reconstructed multi-physics fields, including the fast flux, thermal flux, and power rate distributions, using observations from a single field, such as the thermal flux.

Numerical tests based on the IAEA benchmark demonstrated the efficiency of the proposed method. Three main conclusions can be drawn from the analysis of the numerical results.

(i)   V-CNN can reconstruct the multi-field using observations only from thermal flux;
(ii) All the reconstruction errors in average are below 5%, which is satisfactory for engineering applications;
(iii) Even with a vibration amplitude of $\delta = 5$ cm for sensors, V-CNN exhibits satisfactory performance.

In this study, the original CNN framework was used for image processing and was adapted for field reconstruction with rectangular mesh division. Field reconstruction with an irregular mesh requires additional mesh mapping to map the irregular mesh to a rectangular mesh. The adaptability of the proposed method to various reactor configurations is a continuation of this study.

This study provides a novel approach for field reconstruction using vibration sensors. Future work could highlight the uncertainty quantification of V-CNN considering observation noise systematically and proceed to practical
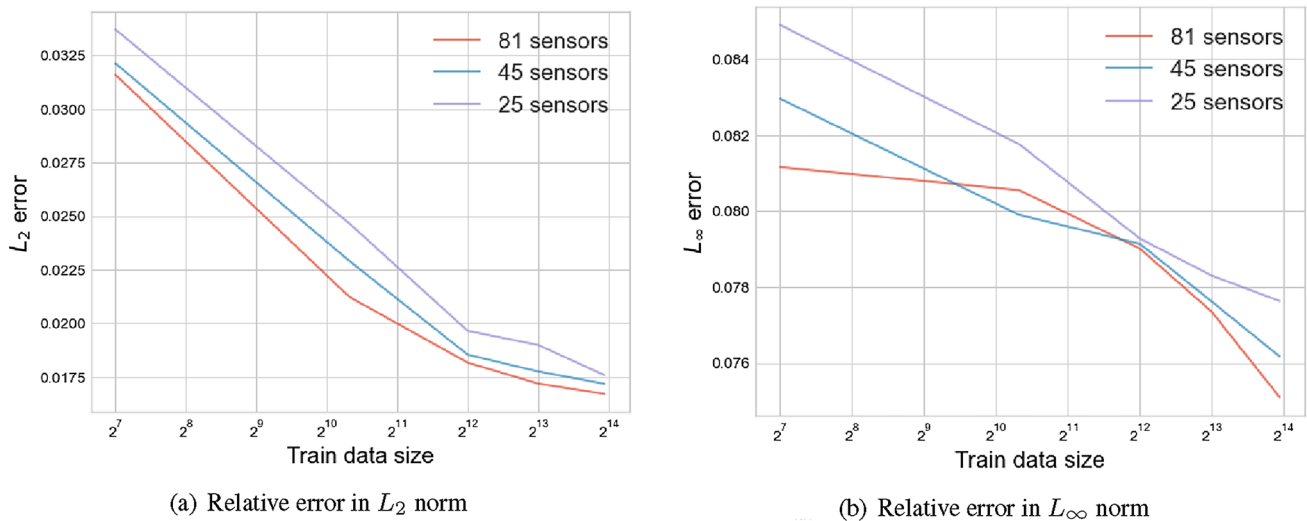
(a) Relative error in L_2 norm

(b) Relative error in L_∞ norm

Fig. 8 Dependence of the relative reconstruction errors in the L_2 and L_∞ norms on the number of training snapshots $n_{\text{snapshot}} = 128, 1280, 4096, 8192, 15743$ and the number of observations $n_{\text{obs}} = 25, 45, 81$ for recovering the thermal flux ϕ_2

Table 6 Dependence of the relative reconstruction errors in the L_2 and L_∞ norms of the noise level σ for recovering the thermal flux ϕ_2

Noise level	$E(e_2(\phi))$	$E(e_\infty(\phi))$
0.0	0.0213	0.1219
0.01	0.0493	0.2956
0.02	0.0510	0.2975
0.03	0.0536	0.3013
0.04	0.0572	0.3078
0.05	0.0616	0.3158

engineering applications based on real nuclear reactors such as the HPR1000 reactor developed in China [58]. In this aspect, data uncertainty could be evaluated using a probabilistic neural network [59] or Bayesian neural network [60]in combination with V-CNN, while the epistemic uncertainty of the model could be examined using the Gaussian stochastic weight averaging technique [61] or other techniques.

To investigate the adaptability of the proposed method to an HPR1000 reactor, a pin-wise field calculation is necessary to consider the fuel and sensor vibrations, which is now being performed by our group. However, in practical engineering cases, the vibrations of reactor components, such as fuel and in-core sensors, lead to complex phenomena in the core. Many studies [2–6] have analyzed the induced variation of neutronic fields (also called neutron noise), considering the induced variation in the cross section parameters of the neutron diffusion equations. Inspired by the neutron noise analysis process, a synthetic modeling approach is necessary for considering the effects of component vibrations. This approach is useful for clarifying the interplay

or distinguish between field reconstructions using in-core sensor vibrations and general reactor noise analyses.

In addition, the combination of V-CNN and fault diagnosis [62] is a possible future research topic. With the development of machine learning in the field of nuclear physics [63, 64], the adoption of V-CNNs in nuclear physics, where CNNs are used [65–67], is also worth investigating.

Author contributions HLG and SBC performed the research. HLG generated data. SBC designed the code. HLG analyzed the data. HLG wrote and revised the manuscript. HL evaluated the robustness of this method. All the authors reviewed the manuscript.

Declarations

Conflict of interest The authors declare that they have no Conflict of interest.

References

1. IAEA-PRIS, Nuclear Power Reactors in the World, no. 2 in Reference Data Series, (International Atomic Energy Agency, Vienna, 2022)

2. I. Pázsit, G.T. Analytis, Theoretical investigation of the neutron noise diagnostics of two-dimensional control rod vibrations in a PWR. Ann. Nucl. Energy **7**, 171–183 (1980). https://doi.org/10.1016/0306-4549(80)90082-1

3. M. Seidl, K. Kosowski, U. Schüler et al., Review of the historic neutron noise behavior in German KWU built PWRs. Prog. Nucl. Energy **85**, 668–675 (2015). https://doi.org/10.1016/j.pnucene.2015.08.016

4. A. Mylonakis, P. Vinai, C. Demazière, Core sim+: a flexible diffusion-based solver for neutron noise simulations. Ann. Nucl. Energy **155**, 108149 (2021). https://doi.org/10.1016/j.anucene.2021.108149

5. A. Vidal-Ferràndiz, D. Ginestar, A. Carreño et al., Modelling and simulations of reactor neutron noise induced by mechanical vibrations. Ann. Nucl. Energy **177**, 109300 (2022). https://doi.org/10.1016/j.anucene.2022.109300

6. P. Vinai, H. Yi, C. Demazière et al., On the simulation of neutron noise induced by vibrations of fuel pins in a fuel assembly. Ann. Nucl. Energy **181**, 109521 (2023). https://doi.org/10.1016/j.anucene.2022.109521

7. C. Demazière, P. Vinai, M. Hursin et al., in *Proceedings of the International Conference on the Physics of Reactors–Reactor Physics paving the way towards more efficient systems* (PHYSOR2018), Cancun, Mexico, Overview of the CORTEX project (2018)

8. S.A. Skidmore, D.J. Krieg, BEACON^TM Core Monitoring and Analysis for Operations of the Westinghouse AP1000. in *Proceedings of the GLOBAL 2009 congress—The Nuclear Fuel Cycle: Sustainable Options and Industrial Perspectives*, France (2009) p. 567

9. H. Gong, Y. Yu, Q. Li et al., An inverse-distance-based fitting term for 3D-Var data assimilation in nuclear core simulation. Ann. Nucl. Energy **141**, 107346 (2020). https://doi.org/10.1016/j.anucene.2020.107346

10. M. Makai, J. Végh, Reactor core monitoring: background, theory and practical applications. Lecture Notes in Energy **58** https://doi.org/10.1007/978-3-319-54576-9

11. J. Fu, S. Cui, S. Cen et al., Statistical characterization and reconstruction of heterogeneous microstructures using deep neural network. Comput. Methods Appl. Mech. Eng. **373**, 113516 (2021). https://doi.org/10.1016/j.cma.2020.113516

12. J. Fu, D. Xiao, D. Li et al., Stochastic reconstruction of 3d microstructures from 2d cross-sectional images using machine learning-based characterization. Comput. Methods Appl. Mech. Eng. **390**, 114532 (2022). https://doi.org/10.1016/j.cma.2021.114532

13. E. Kalnay, *Atmospheric Modeling, Data Assimilation and Predictability* (Cambridge University Press, Cambridge, 2003). https://doi.org/10.1198/tech.2005.s326

14. M. Asch, M. Bocquet, M. Nodet, Data Assimilation: Methods, Algorithms, and Applications (SIAM, 2016). https://doi.org/10.1137/1.9781611974546.bm

15. S. Cheng, J.P. Argaud, B. Looss et al., Background error covariance iterative updating with invariant observation measures for data assimilation. Stoch. Environ. Res. Risk Assess. **33**, 2033–2051 (2019). https://doi.org/10.1007/s00477-019-01743-6

16. O. Goux, S. Gürol, A.T. Weaver et al., Impact of correlated observation errors on the conditioning of variational data assimilation problems. Numer. Linear Algebra Appl. **2**, 529 (2023). https://doi.org/10.1002/nla.2529

17. J.P. Argaud, B. Bouriquet, P. Erhard et al., Data assimilation in nuclear power plant core. Prog. Ind. Math. ECMI **2008**, 401–406 (2010). https://doi.org/10.1007/978-3-642-12110-4_61

18. B. Bouriquet, J.P. Argaud, R. Cugnart, Optimal design of measurement network for neutronic activity field reconstruction by data assimilation. Nucl. Instrum. Methods Phys. Res. Sect. A **664**, 117–126 (2012). https://doi.org/10.1016/j.nima.2011.10.056

19. A. Ponçot, J.P. Argaud, B. Bouriquet et al., Variational assimilation for xenon dynamical forecasts in neutronic using advanced background error covariance matrix modelling. Ann. Nucl. Energy **60**, 39–50 (2013). https://doi.org/10.1016/j.anucene.2013.04.026

20. B. Bouriquet, J.P. Argaud, P. Erhard et al., Nuclear core activity reconstruction using heterogeneous instruments with data assimilation. EPJ Nucl. Sci. Technol. **1**, 18 (2015). https://doi.org/10.1051/epjn/2015-50046-1

21. H. Gong, S. Cheng, Z. Chen et al., An efficient digital twin based on machine learning SVD autoencoder and generalised latent assimilation for nuclear reactor physics. Ann. Nucl. Energy **179**, 109431 (2022). https://doi.org/10.1016/j.anucene.2022.109431

22. J.P. Argaud, B. Bouriquet, F. de Caso et al., Sensor placement in nuclear reactors based on the generalized empirical interpolation method. J. Comput. Phys. **363**, 354–370 (2018). https://doi.org/10.1016/j.jcp.2018.02.050

23. H. Gong, Y. Yu, Q. Li, Reactor power distribution detection and estimation via a stabilized gappy proper orthogonal decomposition method. Nucl. Eng. Des. **370**, 110833 (2020). https://doi.org/10.1016/j.nucengdes.2020.110833

24. R. Fu, D. Xiao, I. Navon et al., A non-linear non-intrusive reduced order model of fluid flow by auto-encoder and self-attention deep learning methods. Int. J. Numer. Methods Eng. (2023). https://doi.org/10.1002/nme.7240

25. H. Gong, Z. Chen, Y. Maday et al., Optimal and fast field reconstruction with reduced basis and limited observations: application to reactor core online monitoring. Nucl. Eng. Des. **377**, 111113 (2021). https://doi.org/10.1016/j.nucengdes.2021.111113

26. H. Gong, Z. Chen, Q. Li, Generalized empirical interpolation method with h1 regularization: application to nuclear reactor physics. Front. Energy Res. **9**, 804018 (2022). https://doi.org/10.3389/fenrg.2021.804018

27. D. Xiao, J. Du, F. Fang et al., Parameterised non-intrusive reduced order methods for ensemble Kalman filter data assimilation. Comput. Fluids **177**, 69–77 (2018). https://doi.org/10.1016/j.compfluid.2018.10.006

28. S. Riva, C. Introini, S. Lorenzi et al., Hybrid data assimilation methods, part i: numerical comparison between GEIM and PBDW. Ann. Nucl. Energy **190**, 109864 (2023). https://doi.org/10.1016/j.anucene.2023.109864

29. S. Riva, C. Introini, S. Lorenzi et al., Hybrid data assimilation methods, part ii: application to the DYNASTY experimental facility. Ann. Nucl. Energy **190**, 109863 (2023). https://doi.org/10.1016/j.anucene.2023.109863

30. S. Cheng, J. Chen, C. Anastasiou et al., Generalised latent assimilation in heterogeneous reduced spaces with machine learning surrogate models. J. Sci. Comput. **94**, 11 (2023). https://doi.org/10.1007/s10915-022-02059-4

31. C. Introini, S. Cavalleri, S. Lorenzi et al., Stabilization of generalized empirical interpolation method (GEIM) in presence of noise: a novel approach based on tikhonov regularization. Comput. Methods Appl. Mech. Eng. **404**, 115773 (2023). https://doi.org/10.1016/j.cma.2022.115773

32. C. Introini, S. Riva, S. Lorenzi et al., Non-intrusive system state reconstruction from indirect measurements: a novel approach based on hybrid data assimilation methods. Ann. Nucl. Energy **182**, 109538 (2023). https://doi.org/10.1016/j.anucene.2022.109538

33. S. Cheng, C. Quilodrán-Casas, S. Ouala et al., Machine learning with data assimilation and uncertainty quantification for dynamical systems: a review. IEEE/CAA J. Autom. Sin. **10**, 1361–1387 (2023). https://doi.org/10.1109/JAS.2023.123537

34. Y. Maday, O. Mula, A. Patera et al., The generalized empirical interpolation method: stability theory on Hilbert spaces with an application to the stokes equation. Comput. Methods Appl. Mech. Eng. **287**, 310–334 (2015). https://doi.org/10.1016/j.cma.2015.01.018

35. M.S. Terman, N.M. Kojouri, H. Khalafi, Optimal placement of fixed in-core detectors for tehran research reactor using information theory. Prog. Nucl. Energy **106**, 300–315 (2018). https://doi.org/10.1016/j.pnucene.2018.03.012

36. V. Yellapu, A. Tiwari, S. Degweker, Application of data reconciliation for fault detection and isolation of in-core self-powered neutron detectors using iterative principal component test. Prog. Nucl. Energy **100**, 326–343 (2017). https://doi.org/10.1016/j.pnucene.2017.04.017

37. B. Anupreethi, A. Gupta, U. Kannan et al., Optimization of flux mapping in-core detector locations in AHWR using clustering approach. Nucl. Eng. Des. **366**, 110756 (2020). https://doi.org/10.1016/j.nucengdes.2020.110756

38. N. Karnik, M.G. Abdo, C.E.E. Perez et al., Optimal sensor placement with adaptive constraints for nuclear digital twins (2023). https://doi.org/10.48550/arXiv.2306.13637.Preprint at arXiv:2306.13637

39. K. Fukami, R. Maulik, N. Ramachandra et al., Global field reconstruction from sparse sensors with Voronoi tessellation-assisted deep learning. Nat. Mach. Intell. **3**, 945–951 (2021). https://doi.org/10.1038/s42256-021-00402-2

40. G. Voronoï, New applications of continuous parameters to the theory of quadratic forms. Z. Reine Angew. Math. **134**, 198 (1908)

41. F. Aurenhammer, Voronoi diagrams-a survey of a fundamental geometric data structure. ACM Comput. Surv. (CSUR) **23**, 345–405 (1991). https://doi.org/10.1145/116873.116880

42. M. Senechal, Mathematical structures: Spatial tessellations. concepts and applications of voronoi diagrams. atsuyuki okabe, barry boots, and kokichi sugihara. wiley, new york, 1992. xii, 532 pp., illus. \$89.95. wiley series in probability and mathematical statistics. Science **260**, 1170–1173 (1993). https://doi.org/10.1126/science.260.5111.1170

43. A. Okabe, B. Boots, K. Sugihara et al., Spatial tessellations: concepts and applications of Voronoi diagrams. (2009). John Wiley & Sons

44. R. Venkatesan, B. Li, *Convolutional Neural Networks in Visual Ccomputing: A Concise Guide* (CRC Press, Boca Raton, 2017). https://doi.org/10.4324/9781315154282

45. S.L. Brunton, B.R. Noack, P. Koumoutsakos, Machine learning for fluid mechanics. Annu. Rev. Fluid Mech. **52**, 477–508 (2020). https://doi.org/10.1146/annurev-fluid-010719-060214

46. V.C. Leite, E. Merzari, R. Ponciroli et al., Convolutional neural network-aided temperature field reconstruction: an innovative method for advanced reactor monitoring. Nucl. Technol. **209**, 645–666 (2023). https://doi.org/10.1080/00295450.2022.2151822

47. V. Nair, G.E. Hinton, in *Proceedings of the 27th International Conference on Machine Learning (ICML-10), Rectified Linear Units Improve Restricted Boltzmann Machines*. 2010, pp. 807–814

48. D.P. Kingma, J. Ba, Adam: a method for stochastic optimization. arXiv preprint arXiv:1412.6980

49. L. Prechelt, Automatic early stopping using cross validation: quantifying the criteria. Neural Netw. **11**, 761–767 (1998). https://doi.org/10.1016/S0893-6080(98)00010-0

50. S.L. Brunton, J.N. Kutz, *Data-Driven Science and Engineering: Machine Learning, Dynamical Systems, and Control* (Cambridge University Press, Cambridge, 2022)

51. G.H. Blaine R, Froehlich R, *Argonne Code Center: Benchmark Problem Book*. Tech. Rep. ANL-7416, Suppl.2. Argonne National Lab.(ANL), Argonne, IL United States. ANL-7416, Suppl.2, (Argonne National Laboratory, 1977)

52. A. Hebert, Applied Reactor Physics, (Presses inter Polytechnique, 2009)

53. S. Marguet, *The Physics of Nuclear Reactors* (Springer, Berlin, 2018). https://doi.org/10.1007/978-3-319-59560-3

54. R. Dautray, J.L. Lions, *Mathematical Analysis and Numerical Methods for Science and Technology: Volume 6 Evolution Problems II* (Springer Science & Business Media, Berlin, 2012)

55. F. Hecht, New development in freefem++. J. Numer. Math. **20**, 251–266 (2012). https://doi.org/10.1515/jnum-2012-0013

56. Z. Wang, A. Bovik, H. Sheikh et al., Image quality assessment: from error visibility to structural similarity. IEEE Trans. Image Process. **13**, 600–612 (2004). https://doi.org/10.1109/TIP.2003.819861

57. P. An, Y. Ma, P. Xiao et al., Development and validation of reactor nuclear design code corca-3d. Nucl. Eng. Technol. **51**, 1721–1728 (2019). https://doi.org/10.1016/j.net.2019.05.015

58. X. Li, Q. Liu, Q. Li et al., 177 core nuclear design for HPR1000. Nucl. Power Eng. **40**(S1), 8–12 (2019). https://doi.org/10.13832/j.jnpe.2019.S1.0008

59. R. Maulik, K. Fukami, N. Ramachandra et al., Probabilistic neural networks for fluid flow surrogate modeling and data recovery. Phys. Rev. Fluids **5**, 104401 (2020). https://doi.org/10.1103/PhysRevFluids.5.104401

60. L. Sun, J.X. Wang, Physics-constrained Bayesian neural network for fluid flow reconstruction with sparse and noisy data. Theor. Appl. Mech. Lett. **10**, 161–169 (2020). https://doi.org/10.1016/j.taml.2020.01.031

61. M. Morimoto, K. Fukami, R. Maulik et al., Assessments of epistemic uncertainty using Gaussian stochastic weight averaging for fluid-flow regression. Phys. D **440**, 133454 (2022). https://doi.org/10.1016/j.physd.2022.133454

62. X.J. Jiang, W. Zhou, J. Hou, Construction of fault diagnosis system for control rod drive mechanism based on knowledge graph and Bayesian inference. Nucl. Sci. Tech. **34**, 21 (2023). https://doi.org/10.1007/s41365-023-01173-8

63. W.B. He, Y.G. Ma, L.G. Pang et al., High-energy nuclear physics meets machine learning. Nucl. Sci. Tech. **34**, 88 (2023). https://doi.org/10.1007/s41365-023-01233-z

64. W.B. He, Q.F. Li, Y.G. Ma et al., Machine learning in nuclear physics at low and intermediate energies. Sci. China Phys. Mech. Astron. **66**, 282001 (2023). https://doi.org/10.1007/s11433-023-2116-0

65. Z. Hui, L. Yu, H. Zhou et al., X-ray crystallography experimental data screening based on convolutional neural network algorithms. Nucl. Tech. **46**, 030101 (2023). https://doi.org/10.11889/j.0253-3219.2023.hjs.46.030101

66. L. Tang, Y. Li, Y.F. Tang, Application of an LSTM model based on deep learning through x-ray fluorescence spectroscopy. Nucl. Tech. **46**, 070502 (2023). https://doi.org/10.11889/j.0253-3219.2023.hjs.46.070502

67. Y.D. Zeng, J. Wang, R. Zhao et al., Decomposition of fissile isotope antineutrino spectra using convolutional neural network. Nucl. Sci. Tech. **34**, 79 (2023). https://doi.org/10.1007/s41365-023-01229-9